ACS APPLIED MATERIALS & INTERFACES

Research Article

www.acsami.org

WO_3-Enhanced TiO_2 Nanotube Photoanodes for Solar Water Splitting with Simultaneous Wastewater Treatment

Karla R. Reyes-Gil* and David B. Robinson

Sandia National Laboratories, P.O. Box 969, Livermore, California 94551-MS9403, United States

Supporting Information

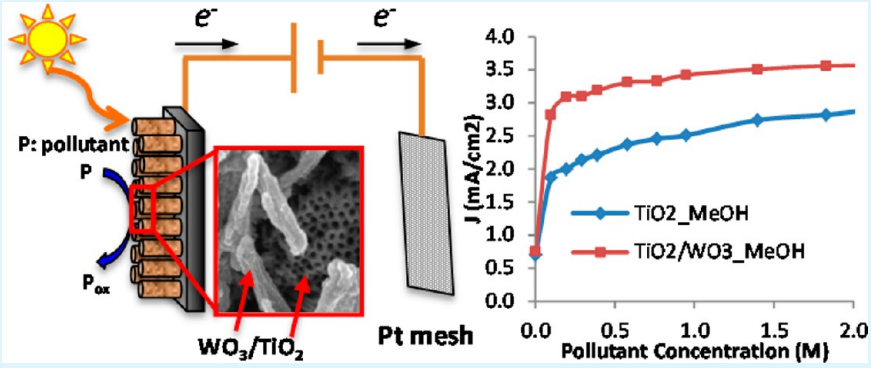

ABSTRACT: Composite WO_3/TiO_2 nanostructures with optimal properties that enhance solar photoconversion reactions were developed, characterized, and tested. The TiO_2 nanotubes were prepared by anodization of Ti foil and used as substrates for WO_3 electrodeposition. The WO_3 electrodeposition parameters were controlled to develop unique WO_3 nanostructures with enhanced photoelectrochemical properties. Scanning electron microscopy (SEM) images showed that the nanomaterials with optimal photocurrent density have the same ordered structure as TiO_2 nanotubes, with an external tubular nanostructured WO_3 layer. Diffuse reflectance spectra showed an increase in the visible absorption relative to bare TiO_2 nanotubes and in the UV absorption relative to bare WO_3 films. Incident simulated solar photon-to-current efficiency (IPCE) increased from 30% (for bare WO_3) to 50% (for tubular WO_3/TiO_2 composites). With the addition of diverse organic pollutants, the photocurrent densities exhibited more than a 5-fold increase. Chemical oxygen demand measurements showed the simultaneous photodegradation of organic pollutants. The results of this work showed that the unique structure and composition of these composite WO_3/TiO_2 materials enhance the IPCE efficiencies, optical properties, and photodegradation performance compared with the parent materials.

KEYWORDS: *TiO_2 nanotubes, WO_3, photodegradation, water splitting, H_2 production, water pollutants*

1. INTRODUCTION

Solar energy is potentially clean, safe, and limitless, but its use at the global scale would benefit from efficient conversion of the energy into a fuel to allow storage and distribution. For solar photoconversion, specialized semiconductors are needed to absorb sunlight and use this energy to drive photochemical reactions. Metal oxides, in particular TiO_2 and WO_3, have properties such as electronic band structure, high photoactivity, chemical stability, and low cost that make them good candidates for photoanodic reactions in aqueous electrolytes. However, the efficiency of these materials is still too low for commercial use. There are three factors that are jeopardizing the incident photon-to-current efficiency (IPCE) of metal oxides: (1) poor absorption of solar light, (2) poor charge-carrier transport within the metal oxide, and (3) poor interfacial charge transfer, each represented as an efficiency η in eq 1.

$$\mathrm{IPCE} = \eta_{e^-/h^+} \cdot \eta_{\mathrm{transport}} \cdot \eta_{\mathrm{interface}} \quad (1)$$

As described below, big improvements have been achieved in the efficiency of these processes individually; however, the overall efficiency has not been significantly improved. The modifications to improve one process sometimes jeopardize the other processes. The approach of the present work is to design a solar cell system that corrects each of the limiting factors in a synergistic way. This proposed system uses nanostructured materials as photoanodes in a photoelectrochemical solar cell, where organic pollutants are photodegraded (oxidized) on the photoanode, simultaneously producing a high electron flux to the cathode (photocurrent density) that can be used for H_2 production (Scheme 1). This work focuses on the optimization of the nanostructure of WO_3 on TiO_2 photoanodes to obtain higher solar absorption, higher photocurrent densities, and

Received: August 12, 2013
Accepted: November 6, 2013
Published: November 6, 2013

Scheme 1. Proposed Combined Waste Treatment and Energy-Harvesting Photoelectrochemical Device, Where P Is Organic Pollutants and P_{ox} Is the Oxidized Pollutants

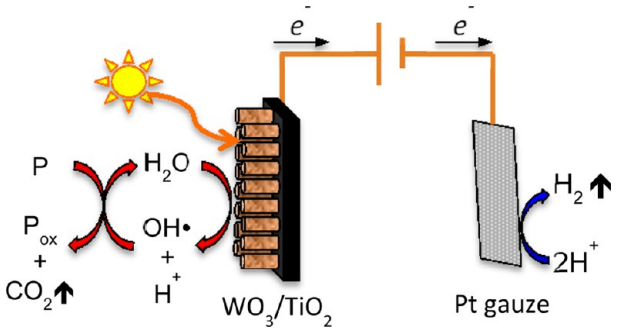

higher photodegradation efficiencies than individual WO_3 and TiO_2 materials.

One of the most studied approaches to increase the visible absorption of metal oxides is compositional doping with anions or transition metals. Due to its electronic bandgap (E_g = 3.2 eV, corresponding to a light wavelength λ = 380 nm), TiO_2 absorbs less than 5% of the natural solar spectrum. Nitrogen doping has been successfully used to increase the visible absorption of TiO_2; however, the efficiency is even worse because N dopants can change the host material crystal structure and act as recombination centers.[1] Another approach to shift the absorption edge toward the visible-light region is coupling TiO_2 with another metal oxide with narrower bandgap, such as WO_3 (E_g = 2.6 eV, corresponding to a light wavelength λ = 477 nm). Contrary to other bandgap narrowing approaches (e.g., doping), the coupling approach is expected to provide a better charge separation, which could also increase the charge transport efficiency.[2]

After the photons are absorbed and electron–hole pairs (e^-/h^+) are created, the next process is the transport of each of the carriers to other phases or regions before recombination occurs. Control over the morphology of absorber materials, to facilitate orthogonalization of charge separation and charge transport, is attracting significant attention for application in solar energy-conversion devices.[3−12] The one-dimensional morphology allows for electrons to move axially along the length of the nanotubes, providing direct and faster electron transport to the back of the contact, while photogenerated holes are separated and collected over relatively short distances in an orthogonal direction.[3−7] In addition, the nanotube architecture has a large internal surface area and can be easily filled with liquid, thus enabling intimate contact with the electrolyte.[1]

Several studies demonstrated that the organized nanostructures enhanced the internal quantum yields and effective minority-carrier diffusion lengths, consequently reducing the electron–hole recombination of metal oxides.[1] However, the photocurrents of nanostructures are limited by low light absorption, so the IPCE values are not significantly improved. Methods of obtaining nearly complete light absorption can be expected to produce very high external quantum yield values for use in optimized solar energy conversion devices.[12] Increasing the optical absorption of films has been a challenge for a number of nanostructured materials, including WO_3.[13−15] A key drawback of WO_3 is that up to now no highly defined tubular structures could be grown, and thus the full potential of WO_3-based nanotubular systems could not be exploited.[13] In contrast, TiO_2 nanotubes have been grown as long as several hundreds of micrometers by anodization.[16,17] In this work, we investigated the use of TiO_2 nanotubes as a skeleton to develop WO_3 nanostructures with long absorption pathways.

When the photogenerated charges reach the electrode/electrolyte interface, they have to be used quickly. Due to rapid recombination of the photogenerated electrons and holes and the slow oxidation of water, it is difficult to achieve stoichiometric water splitting. Sacrificial reagents have been used to react irreversibly with the photogenerated holes, resulting in higher quantum efficiency. The remaining strongly reducing electrons can reduce protons to hydrogen molecules in a process known as nonstoichiometric water splitting. Many organic pollutants in wastewater and biomass are good electron donors and can be used as the donors for electric power generation[18,19] and photocatalytic hydrogen evolution.[20] The overall performance of such devices is limited in part by the solar absorption of the electrode materials.[19]

In this work, we developed a practical synthetic approach to prepare nanostructured WO_3/TiO_2 composite nanotube substrates. The morphology, crystal structure, and optical properties of these new materials were analyzed to find the optimal configuration of each component to obtain higher efficiencies. Diffuse reflectance spectra of tubular nanostructured WO_3/TiO_2 showed an improvement in the visible absorption relative to bare TiO_2 nanotubes and in the UV absorption relative to bare WO_3 films. Photoelectrochemical studies were conducted by employing these materials as photoanodes and measuring the electron flux to the cathode (photocurrent density). The incident photon-to-current efficiency (IPCE) increased from 30% (for bare WO_3) to 50% (for WO_3/TiO_2 composites) and extended up to the visible region (575 nm). The photocurrent density in the presence of common organic pollutants exhibited more than a 5-fold increase. Chemical oxygen demand (COD) measurements demonstrated a simultaneous photodegradation of those pollutants, reaching 40% removal efficiency after 5 h of illumination.

2. MATERIALS AND PROCEDURES

2.1. Preparation of WO_3/TiO_2 Photoanodes. The fabrication of the WO_3/TiO_2 materials presented here involved two processes. The first process is the preparation of TiO_2 nanotubes by anodization. Ti foil (0.25 mm and 99.7% trace metal basis, Aldrich) was cleaned with acetone, deionized water, and methanol and dried under a stream of N_2 gas. Ti foil was cut in pieces of 2 × 4 cm and used as the anode. The back of the foil was covered with insulating tape. Pt gauze (Aldrich, 100 mesh, 425 mg, 25 mm × 25 mm) was used as the cathode. A Teflon beaker was used, and the electrolyte solution used was NH_4F (0.3 wt %) in an ethylene glycol (EG)–water mixture (ratio of 95:5). The reaction was driven by a dc power supply. All the experiments were carried out at room temperature. The TiO_2 nanotubes used for the following reactions were prepared by a two-step process. In the first step (or pretreatment step), a Ti foil was anodized at 50 V overnight (around 15 h). Then, the nanotube layer was removed ultrasonically in deionized water, and the remaining foil was dried under a stream of N_2 gas. In the second step, the pretreated foil was anodized again at 50 V during various time periods between 1 and 5 h. The TiO_2 nanotubes were annealed in air at 500 °C for 2 h.

The second process is the electrodeposition of WO_3 on the TiO_2 nanotubes. The deposition solution was prepared by dissolving Na_2WO_4 salt (Aldrich) in deionized water and

adding concentrated hydrogen peroxide (30%), which can bind to the anion and improve its solubility at low pH. The salt concentration was 25 mM, and hydrogen peroxide concentration was 30 mM. The pH of the resulting solution was 10.4 ± 0.1. Nitric acid was added subsequently to adjust the pH down to 1.4. The solution was prepared the day of the deposition experiments. The electrodeposition experiments were performed in a three-electrode Teflon electrochemical cell at room temperature. The annealed TiO_2 nanotubes were used as a substrate. The reference electrode was Ag/AgCl, and the counter electrode was a platinum gauze. A SP-200 Potentiostat (Bio-Logic Science Instruments) was used to apply a potential of −0.437 V vs Ag/AgCl (−0.24 V vs NHE) and recorded the charge density during the deposition experiments. The resulting composite materials were annealed in air at 400 °C for 2 h.

For comparison purposes, TiO_2 nanoparticle electrodes were made with commercial TiO_2 nanopowder (Degussa P25). An amount of 5 g of TiO_2 P25 was mixed with 0.5 mL of acetic acid and 8 mL of deionized (DI) water, in a ceramic mortar using a pestle and ground for 15 min. TiO_2 P25 paste was spread on conductive fluorine-doped tin oxide film (FTO) on glass. The film was dried at room temperature for 1 h and then annealed in air at 500 °C for 2 h.

2.2. Characterization. The samples on the foil were analyzed by scanning electron microscopy−energy-dispersive X-ray spectroscopy (SEM−EDS) and X-ray diffraction (XRD). Morphological characterization was carried out on a JEOL JSM7600F Thermal Field Emission SEM. Top views of the TiO_2 nanotubes were taken before and after WO_3 electroplating. For the cross-sectional views, the foil was bent, and the film was broken and detached from the foil. Several areas of the film were analyzed using an EDS (Oxford XMax with 80 mm^2 detector using a beam voltage of 10 kV) that was coupled to the SEM. Crystal structures were collected by an Empyrean X-ray diffraction spectrometer, and data were analyzed by X'Pert High Score Plus software. For the optical properties, the absorption spectra of the films were collected using a Shimadzu UV-2101PC spectrometer with a diffuse reflectance adapter.

2.3. Photoelectrochemical and Photodegradation Analysis. For photoelectrochemical measurements, the back of the foil was gently polished to remove any oxides. Conductive silver epoxy was then used to attach a copper wire to the back of the foil. The metallic contact and the foil edges were then covered with Hysol 1C epoxy to produce an exposed area of 0.8−1.2 cm^2. The contact wire was threaded through a glass tube, and the electrode was attached to the end of the tube through the use of Hysol 1C epoxy. The electrodes were allowed to cure for >12 h at 60 °C. The area of the electrode was measured by taking a digital image, using a flatbed scanner, of the electrode and of a calibration scale. The resulting images were analyzed using ImageJ software.

A Teflon electrochemical cell with a quartz window, a platinum foil counter electrode, and Ag/AgCl reference was used for all photoelectrochemical studies. A solar simulator (ABET Technologies, model 10500) with an Air Mass (AM) = 1.5 filter set was used as an illumination source. The intensity of the Xe lamp was measured using a solar power meter (calibrated with a standard Si photodiode), and the incident illumination intensity was adjusted by changing the position of the lamp relative to that of the electrochemical cell. For all the photoelectrochemical experiments, except for IPCE measurements, an intensity of 100 mW/cm^2 (equivalent to 1 sun) was used to illuminate the cell. No correction was made for optical reflection and scattering losses, but it is expected that some of the light intensity is lost when the light goes through the quartz window and the electrolyte before reaching the electrode. The electrolyte was aqueous 0.10 M H_2SO_4 (pH = 1.4) for all experiments. A typical volume used was 40 mL. Electrochemical measurements were recorded using an SP-200 potentiostat (Bio-Logic Science Instruments). Photocurrent densities were calculated as the difference between currents (corrected for the electrode area) that were recorded in the presence and absence of illumination, acquired consecutively. For measurements under visible light, a cut-on (λ > 400 nm) filter was used. Methanol, formic acid, formaldehyde, and ethylene glycol were used as organic pollutant models and added to the supporting electrolyte in controlled amounts from 0.1 M up to 3 M depending on the compound solubility.

For IPCE measurements, a monochromator was placed in front of the solar simulator. The data were collected every 25 nm from 300 to 600 nm. The following equation used the IPCE values at each measured wavelength.

$$\mathrm{IPCE} = \frac{J \times 1239.8}{P \times \lambda} \tag{2}$$

where J is the photocurrent density in mA/cm^2; P is the calibrated monochromated illumination power intensity in mW/cm^2; λ is the wavelength in nm at which this illumination power is measured; and 1239.8 in V × nm represents a multiplication of Planck's constant and the speed of light. The peak center and fwhm were determined with a Stellar Net minispectrometer. The fwhm was between 4.5 and 7.0 nm. The power intensity was determined before and after each experiment with a Gentec-EO power meter (item number 201751) with a chopper and lock-in amplifier.

For photodegradation analysis, the dichromate chemical oxygen demand (COD) high range method and a COD photometer (HI 83099 from Hanna Instruments) were used to calculate the COD removal efficiency.

$$\text{removal efficiency} = \left(\frac{\mathrm{COD}_{\mathrm{initial}} - \mathrm{COD}}{\mathrm{COD}_{\mathrm{initial}}}\right) \times 100 \tag{3}$$

The photocurrent was measured continuously during the photoelectrochemical degradation experiment. A control experiment was performed using the same methodology, but with no electrodes, to measure the loss of organic pollutants for evaporation. To minimize the evaporation, the quartz beaker was covered with parafilm, and the aliquots at different times were collected using a syringe. An amount of 0.2 mL of the sample was added to the pre-dosed reagent vial (HI 93754C, Hanna Instrument) and mixed by inverting the vial a couple of times. The vials were heated for 2 h at 150 °C in the test tube heater (HI 740216) and then analyzed with the photometer (HI 83099).

3. RESULTS AND DISCUSSION

3.1. Synthesis of Nanostructured WO_3/TiO_2 Nanotubes. In the last decade, several studies demonstrated that organized nanostructures, such as nanorods, nanotubes, and nanowires, improve the charge carrier transport compared to compact electrodes or nanoparticle networks.[21] However, the low surface packing of typical one-dimensional nanostructures affects the absorption at the optical plane.[12] Increasing the optical absorption of films has been a challenge for a number of nanostructured materials. In contrast to TiO_2 nanotubes,[16]

Scheme 2. Two-Step Synthetic Approach to Prepare WO_3/TiO_2 Nanotubes

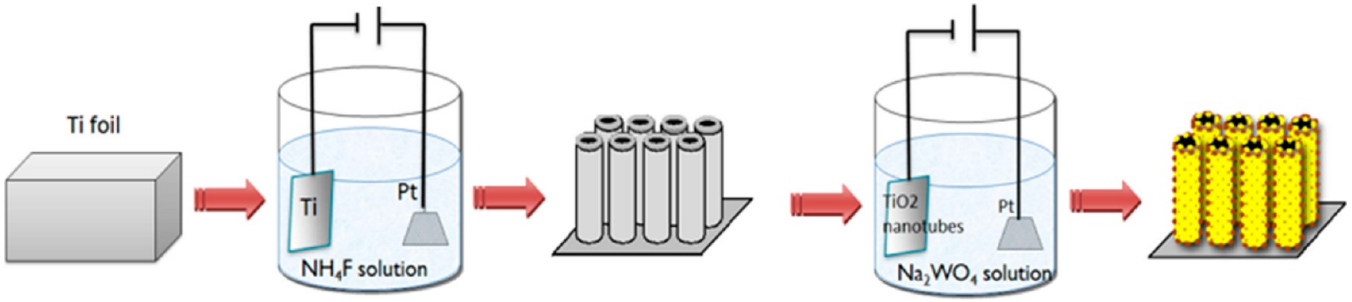

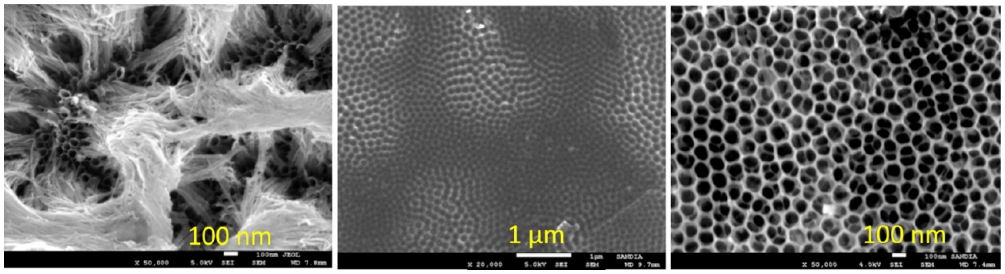

Figure 1. SEM images of TiO_2 nanotubes (left) first anodization, (center) Ti foil after nanotube layer removed, and (right) second anodization.

achieving thick, well-defined, porous WO_3 structures by anodization has been more difficult, due to the solubility of the oxide.[22] The formation of micrometer thick porous WO_3 films (up to 2 μm) has been recently reported by the anodization of W foil.[22] Optimization studies of anodization parameters indicated that longer anodization times yielded thicker porous layers, but at the same time, the pore diameter increased, reducing the packing fraction.[12] The development of synthetic methods for achieving nearly complete light absorption is thus needed to develop more efficient nanostructured photoelectrodes from this material system.

A strategy explored by Benoit et al. dip coats TiO_2 nanotubes (NTs) with a solution of WCl_6 to get, after annealing, an inhomogeneous coating of monoclinic WO_3 on the surface of the NT array.[13] Lai et al. sputter deposited W onto a TiO_2 NT array. At low sputtering power (<180 W), TiO_2 nanotubes preserved the high-ordered structures. However, at higher power (>180 W) the nanotubes collapsed.[23] Nah et al. showed that composite TiO_2–WO_3 NTs can be fabricated by anodization of a TiW alloy.[14] Park et al. prepared a WO_3-coated TiO_2 nanotube array by electrochemical deposition of WO_3 sol to TiO_2 nanotube array. Somasundaram et al. prepared WO_3/TiO_2 composite films by sequential deposition of WO_3 and TiO_2 from two separate baths containing the tungsten and titanium precursor species, respectively.[24] All these previous attempts produced TiO_2 nanotubes decorated with thin WO_3 nanoparticle layers, although WO_3 did not show any organized structure by itself.

The synthetic approach of this work is to increase the absorption pathway of WO_3 nanostructures using TiO_2 nanotubes as a support structure (or skeleton). Scheme 2 shows the two-step process synthesis developed to prepare the composite materials. In the first step, TiO_2 nanotubes were prepared by anodization of Ti foil. Then the nanotubes were used as a substrate for WO_3 electrodeposition in the second step.

3.1.1. TiO_2 Nanotube Anodization. The SEM image (Figure 1, left) showed that after the first anodization the TiO_2 nanotubes are in a disordered array due to the corrugated surface of the Ti foil. After the nanotube layer was removed ultrasonically, an imprint pattern was left on the foil (Figure 1, center), which acts as a template in the further growth of well-aligned nanotubes (Figure 1, right). The nanotubes are highly uniform and vertically oriented with an opening (mouth) of 100 nm in diameter and walls with a thickness of around 10 nm. The length of the nanotubes is proportional to the anodization time. For anodization times of 1, 2, and 5 h, the length of the nanotubes according to SEM cross-sectional images was 6, 12, and 20 μm, respectively. According to previous studies, TiO_2 nanotubes with a length between 15 and 20 μm showed the highest photoactivity.[1] For that reason, the composite materials were prepared using TiO_2 nanotubes anodized for 5 h.

3.1.2. WO_3 Electrodeposition. High-quality WO_3 films are most generally obtained by vacuum evaporation and sputtering. Unfortunately, these methods are time consuming and expensive. Wet low-cost methods, such as electrodeposition, seem to be a promising approach to create WO_3 films. The film electrodeposition method is based on the cathodic reduction of a peroxo precursor, which is obtained by mixing a tungsten precursor with an excess of hydrogen peroxide. The precursor is described as a dimer with the formula $W_2O_{11}^{2-}$ with a peroxide (O_2) ligand.[25] The oxidation state of W is +6. The deposition reaction is described as

$$W_2O_{11}^{2-} + (2 + x)H^+ + xe^- \rightarrow 2WO_3 + (2 + x)/2H_2O + (8 - x)/4O_2$$

It has been shown that parallel parasitic reactions take place and should correspond to hydrogen evolution, colloidal WO_3 formation, and reduction of free H_2O_2, residual O_2, and polytungstate.[25] Due to all the parasitic reactions and uncertainty of the deposition efficiency and stoichiometry, we report deposited amounts in deposited charge density (mAh) instead of moles.

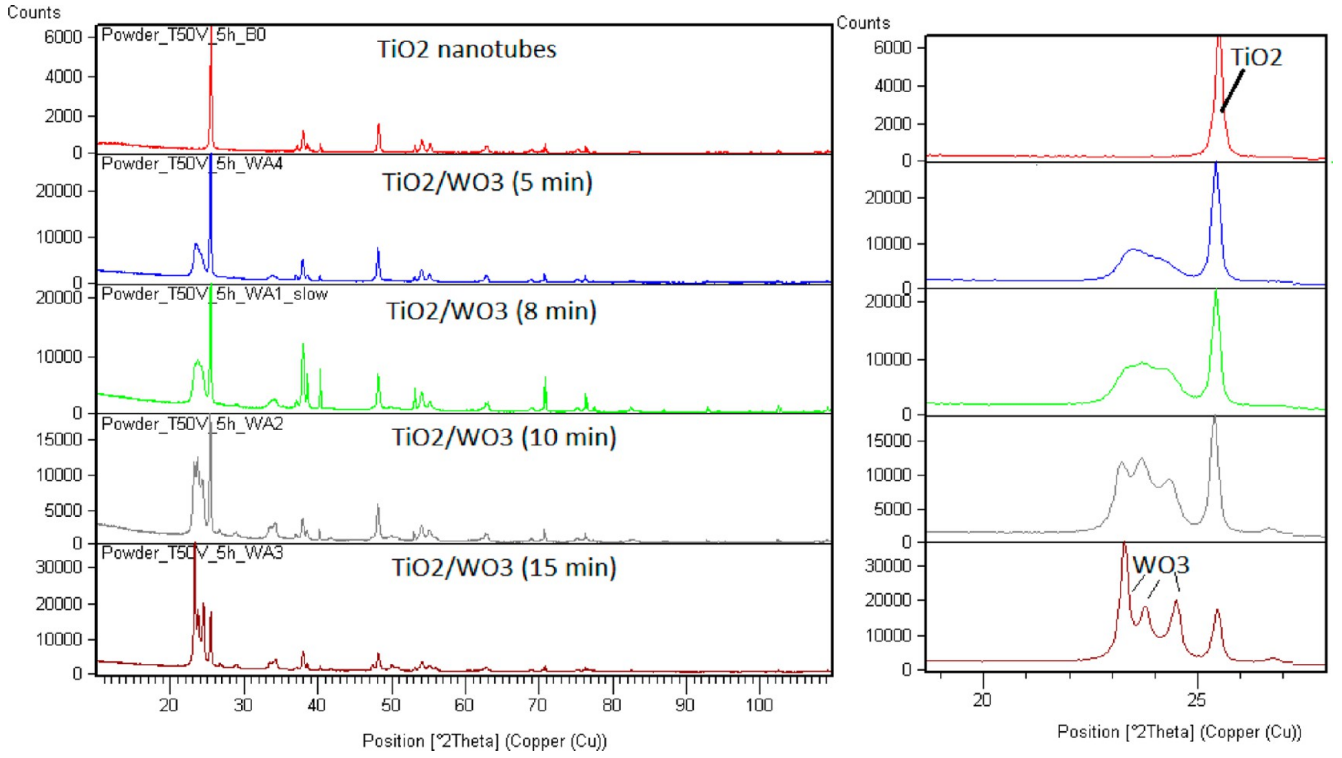

Figure 2. XRD patterns of TiO_2 and WO_3/TiO_2 composite materials at a wide (left) and narrow (right) range of 2θ values.

Annealed TiO_2 nanotubes were used as a substrate for WO_3 electrodeposition. The annealing of TiO_2 is needed before the deposition experiments because amorphous TiO_2 partially dissolved in the tungstic acid solution. We observed that WO_3 electrodeposition on flat substrates suffers adhesion problems. The WO_3 control samples prepared on Ti foil or FTO glass were spontaneously separated from the substrate after being tested in the electrochemical cell. However, using nanotubes as a substrate, WO_3 samples showed excellent adhesion and connectivity to the substrate and excellent structural stability. In addition, this synthesis offers an easy control of the morphology through the synthetic parameters. For instance, the length of the TiO_2 nanotubes can be controlled by the anodization time, and the WO_3 nanostructures can be modified by the electrodeposition time. We expect that this process will allow for low-cost manufacturing, can be easily scaled-up to produce larger samples, and can be adapted for the preparation of other composite nanostructured materials.

3.2. Characterization of Nanostructured WO_3/TiO_2 Nanotubes. *3.2.1. Crystal Structure and Composition.* Figure 2 shows the X-ray diffraction (XRD) patterns of WO_3/TiO_2 composite films that had been annealed at 400 °C in air for 2 h, as a function of the WO_3 electrodeposition time. TiO_2 nanotubes show the distinct peaks of the anatase phase. No other XRD peaks except for Ti foil peaks were detected, indicating the presence of a single type of crystalline compound. After the WO_3 electrodeposition, the films showed three additional distinct peaks in the range $23° < 2\theta < 25°$ indicating that the samples are composed of TiO_2 and WO_3. The three peaks are more defined as the electrodeposition time increases. WO_3, despite its simple stoichiometry, can be found in a large variety of crystal structures (e.g., monoclinic, orthorhombic, and triclinic).[26,27] Comparing the XRD patterns with the JCPD reference files, the diffraction peaks resemble those of a monoclinic structure (JCPD # 43-1035), the most stable phase at room temperature, and a photoactive phase of WO_3.[28,29] No additional peaks were detected, indicating the absence of crystalline Ti−W alloys.

EDS was performed in at least five different areas in the same sample to accurately represent the whole sample. The main elements found in the samples were titanium, oxygen, and tungsten (S-1). Trace amounts of gold were detected because gold was sputtered on the sample to avoid charging. Table 1 summarizes the atomic percentages (at %) determined by averaging EDS data in several represented zones in the samples. As expected, the W atomic percent increases, and the Ti atomic percent decreases as the electrodeposition time increases.

Table 1. Average Atomic Percentages (at %) of the Main Elements Found in EDS Spectra

sample	charge density (mA h/cm^2)	O (at %)	Ti (at %)	W (at %)
TiO_2	----	72	28	0
TiO_2/WO_3 (5 min)	0.130	69	21	10
TiO_2/WO_3 (10 min)	0.225	71	15	14
TiO_2/WO_3 (15 min)	0.302	73	8	19

3.2.2. Optical Properties. Figure 3 shows the UV and visible absorption of WO_3/TiO_2 composites, TiO_2 nanotubes only, and WO_3 only. TiO_2 nanotubes showed an almost complete absorbance of UV light up to 375 nm. WO_3 nanoparticles absorbed less than half of the incident light up to 480 nm. WO_3/TiO_2 nanotubes absorb almost all the UV light and extend the absorption up to the visible region. Diffuse reflectance spectra showed an improvement in the visible

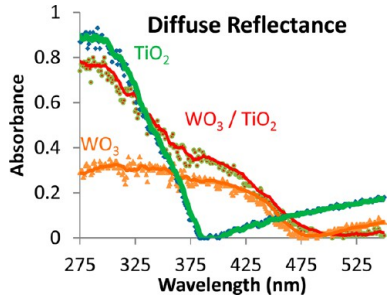

Figure 3. Absorption spectra of WO_3 (orange curve), TiO_2 nanotubes (green curve), and WO_3/TiO_2 materials (green curve).

absorption relative to bare TiO_2 nanotubes and more than twice the UV absorption relative to WO_3 nanoparticles.

Diffuse reflectance spectra shown in Yang's work demonstrated that WO_3 materials with no defined morphology absorbed only 30% of the UV light, agreeing with our diffuse reflectance data for pure WO_3.[30] Optimizing the texture and thickness (~2.8 μm) of WO_3 materials, the UV absorption was 50%, keeping the same absorption onset. The authors attributed this 20% improvement to light scattering within the textured film. Our previous work showed that WO_3 nanopores absorbed less than half of the incoming UV light.[12] This low light absorption was the limiting factor for the photoconversion performance. The WO_3/TiO_2 composite materials reported in this work absorbed almost 80% of the incident UV light, which is equivalent to a 50% improvement relative to nontextured WO_3 materials, but keeping the same absorption onset on the visible region ($\lambda \approx 500$ nm). We attribute this absorption improvement in part to the longer absorption pathways of the nanostructures.

3.2.3. Morphology. The morphology of the photoelectrodes plays an important role in their performance. In particular, several studies demonstrated that organized nanostructures could improve the minority-carrier transport and reduce electron/hole recombination. In this section, we will discuss how the synthetic parameters change the morphology of WO_3. The WO_3 electrodeposition on a flat Ti foil produced a compact layer with some visible cracks (S-2). In contrast to flat substrates, the nanotubes serve as a skeleton to create thick nanostructured WO_3 materials with long absorption pathways. SEM images (Figure 4) show different nanostructures as a function of WO_3 electrodeposition time. These results show that the substrate determines the morphology of the electrodeposited WO_3 material.

Figure 4 shows the evolution of WO_3 materials during the synthetic process. At the beginning of the electrodeposition process, the WO_3 particles were deposited around the TiO_2 nanotube walls. After 10 min of reaction, WO_3 tubular nanostructures grew on top of the TiO_2 nanotubes. After 15 min, a cracked compact WO_3 layer was developed, covering the WO_3 nanostructures and TiO_2 nanotubes. As can be seen in Figure S-3 (Supporting Information), it has a multilayer structure, where the bottom is the TiO_2 nanotubes on Ti foil, the middle is WO_3 tubular nanostructures, and the top is the WO_3 compact layer. The TiO_2 nanotubes look unclogged suggesting that WO_3 nanostructures are located on top of the TiO_2. SEM images thus demonstrate that these composite WO_3/TiO_2 materials have the same ordered structure as TiO_2 nanotubes with an external WO_3 layer and that TiO_2 nanotubes act as a skeleton to create defined nanostructures.

3.3. Effect of the Morphology in the Solar Photoresponse. Photoelectrochemical performance of these composite materials has been investigated by employing them as photoanodes in the photoelectrochemical cell in a water-splitting reaction, oxidizing water to H^+ and such species as oxygen or peroxide and at the photoanode, and reducing H^+ to hydrogen at the platinum cathode. For comparison purposes, WO_3, TiO_2 nanotubes, and TiO_2 nanoparticles (P25) were also tested under the same conditions. The performance of WO_3/TiO_2 materials with different morphology was evaluated under visible light (Figure 5). Pure TiO_2 has very little visible induced photocurrent. WO_3/TiO_2 materials with low WO_3 concentration (5 min electrodeposition time) show similar response as

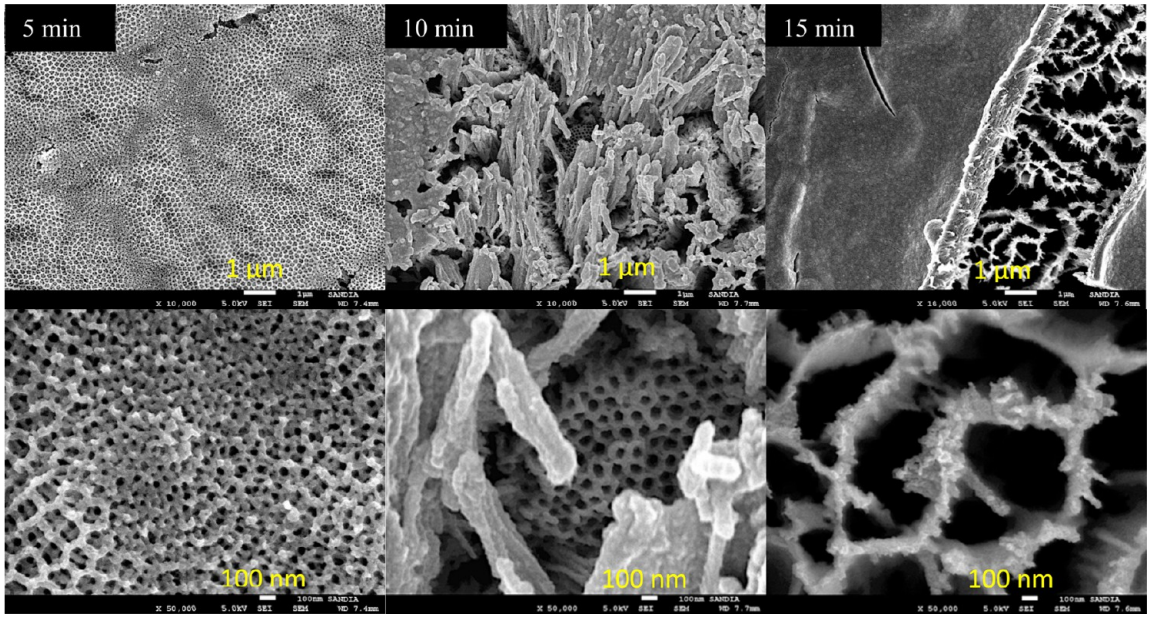

Figure 4. SEM images of WO_3/TiO_2 materials as a function of electrodeposition time: 5, 10, and 15 min. Images in the first row were taken at 10K× magnification and in the second row at 50K× magnification.

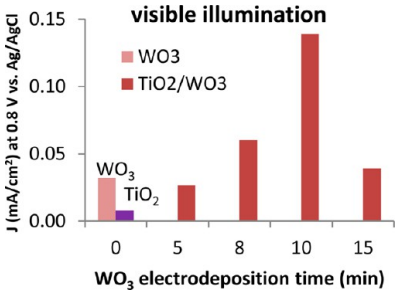

Figure 5. Photocurrent density under visible light (λ > 400 nm) as a function of WO_3 electrodeposition time. Photocurrent density of bare WO_3 and TiO_2 NT was included for comparison purposes. A constant voltage of 0.8 V vs Ag/AgCl was applied.

pure WO_3. As the electrodeposition time increases, the visible induced current also increases, until a sudden decrement at higher concentration. As shown previously in Figure 4, the morphology of the materials changes with the electrodeposition time. The WO_3 tubular nanostructures prepared at 10 min electrodeposition time obtained higher photocurrent densities. The reduction in photocurrent at higher concentration is probably due to the compact layer created on the top, which could act as recombination centers or limit the effective electrode area. The photogenerated e^-/h^+ pair would probably recombine in this compact layer before they can reach the organized nanostructures.

3.4. Incident Photon to Current Efficiency. An important measurement is the IPCE, which determinates the ratio of the incident photons that are successfully converted into photocurrent as a function of wavelength. If we compare the same bulk material in the same electrolyte, keeping constant everything except the morphology, then we can obtain information about how morphology affects the IPCE. Figure 6 shows the incident photon to current efficiency (IPCE) at 0.8

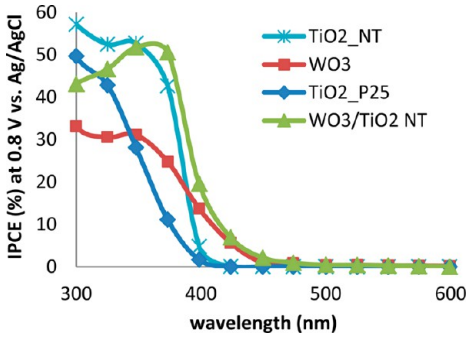

Figure 6. IPCE as a function of wavelength of WO_3 (square red markers), TiO_2 nanotubes (asterisk aqua markers), TiO_2 nanoparticles (diamond blue markers), and WO_3/TiO_2 (triangle green markers) electrodes. A constant voltage of 0.8 V vs Ag/AgCl was applied.

V vs Ag/AgCl as a function of wavelength with no cocatalyst or sacrificial reagent added to the electrolyte. TiO_2 nanotubes and TiO_2 nanoparticles (P25) have the same onset, which is primarily determined by the bandgap, but the nanotubes showed a faster rise in the efficiency at decreasing wavelength. As the bandgap and the interface are the same for both electrodes, this improvement can be attributed primarily to the enhanced charge carrier transport due to the organized one-dimensional nanostructures. WO_3 film obtained ~30% efficiency in the UV region, while TiO_2 obtained more than 50% efficiency. The efficiency onset for WO_3 and TiO_2 electrodes was 550 and 400 nm, respectively.

In the case of the composite WO_3/TiO_2 nanotubes, the IPCE response has the same onset as WO_3 materials but a fast rise in the efficiency toward the UV region similar to TiO_2 nanotubes. Comparing WO_3/TiO_2 nanotubes with the individual materials, Figure 6 shows that coupling TiO_2 with WO_3, a semiconductor with narrower bandgap, produces a red-shift in the IPCE response. Also, WO_3/TiO_2 nanotubes have a higher UV response compared to WO_3 materials. There is not a unique mechanism to explain these results. According to multiple studies of nanotubes, this improvement could be attributed in part to better absorption and to better charge transport due to the organized nanostructures.[3−12] In addition, it has been reported that the electron transfer from TiO_2 to WO_3 results in effective electron−hole separation, which could improve the IPCE values as well.[21] Composite WO_3 and TiO_2 materials have shown a favorable electron injection from the conduction band of TiO_2 to that of WO_3 and hole transfer between valence bands in the opposite direction, which reduce e^-/h^+ recombination in both semiconductors.[31] Somasundaram et al. reported IPCE values of <20 % for WO_3 films and <37% for WO_3/TiO_2 composite materials at 0.8 V vs Ag/AgCl.[24] The authors attributed this improvement to the beneficial effect of electronic junctions between the WO_3 and TiO_2 components in terms of spatially separating the photogenerated e^-/h^+ pairs.

3.5. Photoelectrochemical Properties of TiO_2 and WO_3/TiO_2 Nanotubes. The photoelectrochemical behavior of TiO_2 and WO_3/TiO_2 nanotube electrodes was determined from current−potential curves obtained in 0.1 M H_2SO_4 and 0.1 M H_2SO_4 + 1 M CH_3OH solutions. Figure 7 and Figure 8 show the photocurrent densities as a function of applied potential. The incident light from a solar simulator was chopped during the potential scan. As can be seen in both figures, the photoresponses are very fast, and the dark currents are insignificant. The shape of the curves is typical of n-type semiconductor behavior. For Figure 8 a cut-off filter was used to pass only visible light (λ > 400 nm).

As shown in Figure 7, the photocurrent onset potential of the WO_3/TiO_2 electrode is more positive than those for the TiO_2 electrode because TiO_2 has a more negative flatband potential.[19] A saturation of photocurrent is observed at +0.3 and +0.7 V (vs Ag/AgCl) for TiO_2 and WO_3/TiO_2 electrodes, respectively. In the case of WO_3, reports showed that control of the film morphology represents a way of optimizing photocurrent yield.[30,32] The authors demonstrated that the photocurrent density applying 1.6 V vs SCE can be enhanced from 0.5 to 2.2 mA/cm^2 because the texture of the material changes.[30] To compare with our composite materials, at 0.8 vs Ag/AgCl (0.753 V vs SCE) the best film reported in Yang's work obtained equivalent to 0.54 mA/cm^2 under AM 1.5 simulated sunlight, and our WO_3/TiO_2 materials showed 0.70 mA/cm^2. Yang et al. attributed the photocurrent improvement to the morphology rather than to a bandgap shift or doping effect. In the case of WO_3/TiO_2 composite materials, the film morphology also dictates the quality of the photoresponse.[22] Somasundaram's work showed that WO_3/TiO_2 materials with layered morphology clearly aid vectorial electron transfer and minimize e^-/h^+ recombination within the film.[24]

3.6. Simultaneous Photodegradation of Organic Pollutants. Sacrificial reagents have been used to react fast and irreversibly with the photogenerated holes resulting in higher quantum efficiency. The electrons from this oxidation

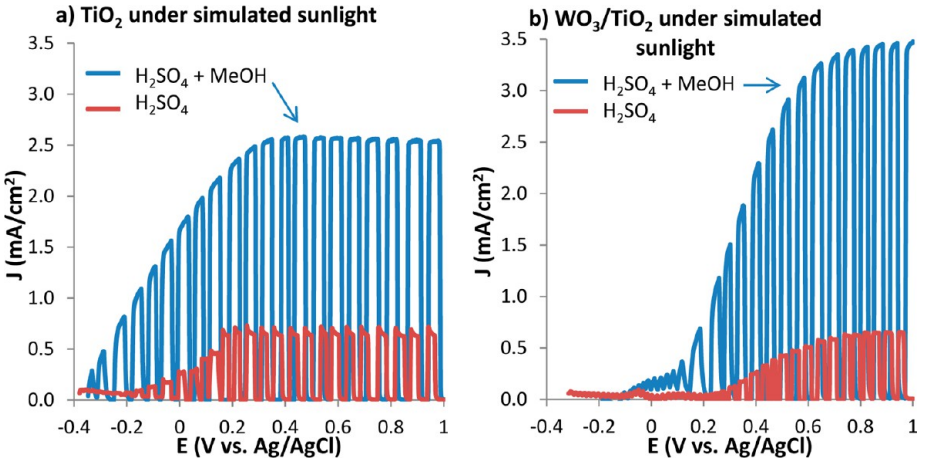

Figure 7. Photocurrent density of (a) TiO_2 NT and (b) WO_3/TiO_2 NT under intermittent simulated sunlight using 0.1 M H_2SO_4 as electrolyte (red curve) and with 1 M methanol added (blue curve).

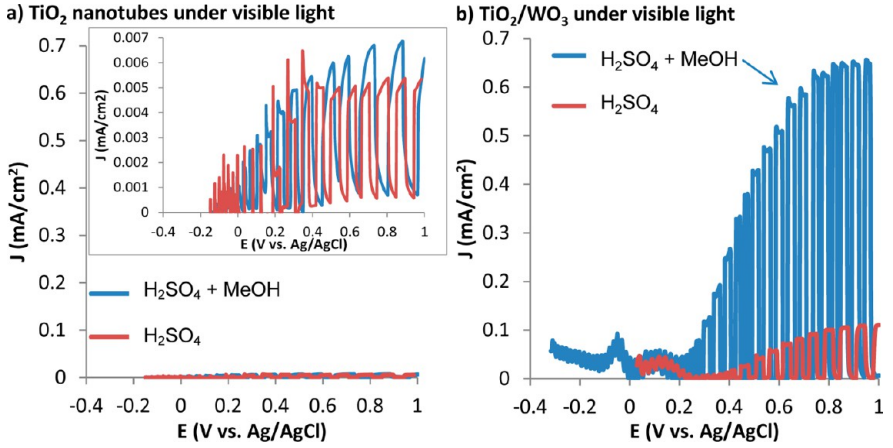

Figure 8. Photocurrent density of (a) TiO_2 NT and (b) WO_3/TiO_2 NT under intermittent visible light (λ > 400 nm) using 0.1 M H_2SO_4 as electrolyte (red curve) and adding 1 M methanol (blue curve).

reaction can reduce protons to hydrogen molecules in a process known as nonstoichiometric water splitting (as shown in Scheme 1). Photocatalytic decomposition of organic pollutants and production of clean hydrogen fuel can take place simultaneously when the pollutants are acting as electron donors.[33,34] Li et al. reported enhanced photocatalytic hydrogen production using aqueous Pt/TiO_2 suspension in the presence of pollutants such as formic acid and formaldehyde, which act as electron donors.[20] Despite the limited work on using pollutants as electron donors, the encouraging results show the promise of the integration of pollutant decomposition and clean hydrogen production.

3.6.1. Addition of Methanol. As a proof of concept, methanol (1 M) was used as a model for organic pollutants and added to the electrolyte. A WO_3/TiO_2 electrode exhibited more than 5-fold increase, reaching a saturated photocurrent density as high as 3.5 mA/cm^2, while TiO_2 NT exhibited a 3.5-fold increase reaching around 2.5 mA/cm^2 (Figure 7). Under visible light (Figure 8), TiO_2 nanotubes obtained very small photocurrent densities, as can be seen in the inset, less than 0.007 mA/cm^2 with no significant improvement with the addition of methanol. However, the WO_3/TiO_2 electrode exhibited an almost 6-fold increase, reaching a saturated photocurrent density of 0.65 mA/cm^2.

It is expected that the addition of methanol induces a doubling of the photocurrent and a reduction of the current onset potential compared with water oxidation alone, as observed in prior work.[35,36] This current doubling can be explained as a two-step sequence, where the first step is the oxidation of substance M (in this case methanol) by a photogenerated hole and the second step is an oxidation of M^+ (photoproduced product) by the release of an electron to the conduction band. The photocurrent doubling effect is the sum of the hole current and the electron current injected into the conduction band. Yang et al. reported a saturated photocurrent about three times higher after the addition of methanol to the electrolyte (equivalent to 2.5 mA/cm^2 at 0.8 vs Ag/AgCl under AM 1.5).[30] The authors suggested that the uniquely textured film might play an important role in the anomalous increases in photocurrent. In our case, the photocurrent density for WO_3/TiO_2 and TiO_2 nanotube electrodes increased by 5-fold and 3.5-fold, respectively, with the addition of methanol. Although further studies are required to fully understand this unusual increase in photocurrent, this is probably due to a combination of multiple factors. In addition to the photocurrent doubling effect observed by Santato et al. and the morphology role observed by Yang, the additional improvement could be attributed to an enhancement of the interface efficiency due to

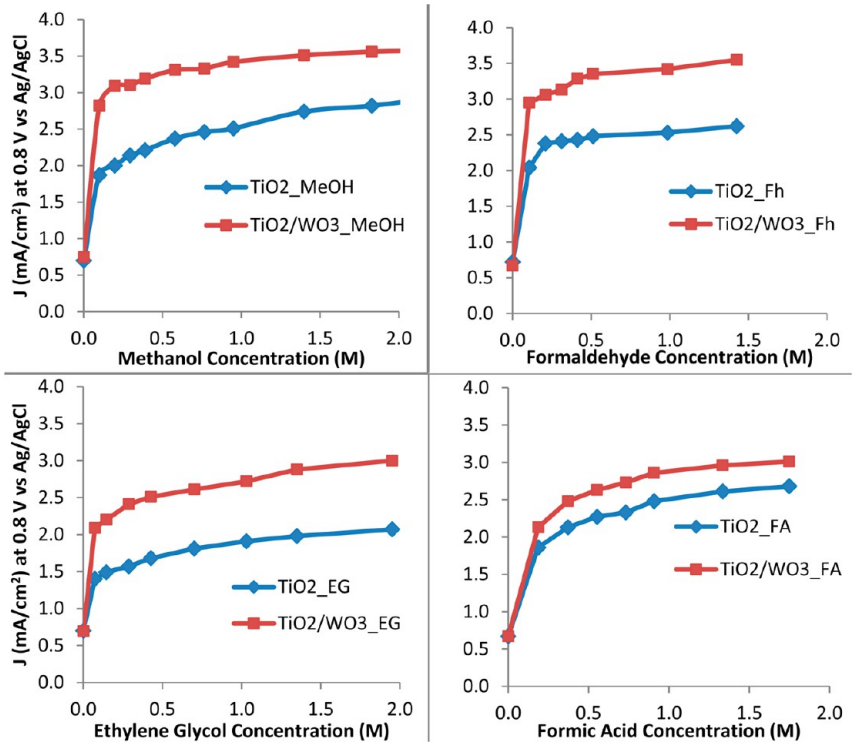

Figure 9. Photocurrent density as a function of different organic compound concentration. All experiments were carried out under constant voltage of 0.8 V vs Ag/AgCl.

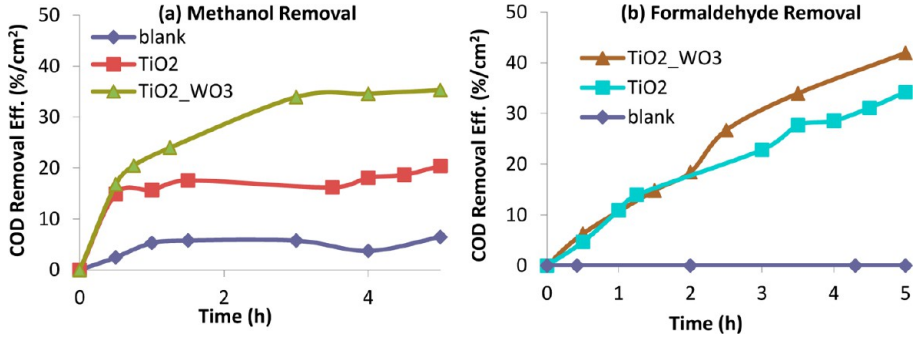

Figure 10. COD removal efficiency of (a) methanol and (b) formaldehyde. All the experiments were carried out under constant voltage of 0.8 V vs Ag/AgCl.

rapid and irreversible consumption of the photogenerated holes, which suppress the e^-/h^+ recombination in the interface.

Another example of improvement in the photocurrent with the addition of methanol was observed for the composite materials relative to TiO_2 nanotubes (approximately 1 mA/cm^2 higher photocurrent densities). As shown in Figure 8, the photoresponse under only visible light increased by more than 6-fold for the composite material with versus without methanol; however, the TiO_2 nanotubes did not show a significant improvement. A moderate improvement in the visible absorption and IPCE values in $\lambda > 400$ nm can make a significant improvement in the solar photocurrent density, considering that 44% of the sunlight is visible and only 3% is UV.

3.6.2. Photocurrent Density As a Function of Different Organic Pollutant Concentration. In addition to methanol, we studied formic acid and formaldehyde, two common organic pollutants found in wood and leather industrial wastewater, and ethylene glycol, a deicing agent found in airport and road drainage. Figure 9 shows the photocurrent density as a function of the concentration of different organic compounds (pollutants). In all the cases, increasing the concentration of the pollutants resulted in an increase of the photocurrent densities. WO_3/TiO_2 electrodes produced higher photocurrent densities compared to bare TiO_2 electrodes. For the WO_3/TiO_2 electrode, as compared to the water splitting case, the photocurrent density exhibited a 5.3-fold increase with formaldehyde, 4.6-fold increase with formic acid, and 4.4-fold increase with ethylene glycol. For the TiO_2 electrode, the photocurrent density exhibited a 4-fold increase with formic acid, 3.6-fold increase with formaldehyde, and 3-fold increase with ethylene glycol. Li and co-authors showed that the efficiency of the electron donors can be correlated with the nature of the interaction between the pollutant and TiO_2 surface sites.[20]

3.6.3. Chemical Oxygen Demand Measurements. Chemical oxygen demand (COD) is used to indirectly measure the amount of organic compounds in surface water and wastewater.

In this work, COD measurements were used to follow the degradation progress of methanol and formaldehyde during the photoreaction. A 0.5 cm^2 electrode was illuminated using a sunlight simulator. The quartz cell was covered with parafilm to minimize evaporation, and aliquots were taken at different times. A control experiment (blank) was performed under the same conditions, except with no electrodes, to determine spontaneous photodegradation. Figure 10 shows COD removal efficiency, calculated according eq 3, as a function of illumination time. The COD initial value was 5000 and 3000 ppm for methanol and formaldehyde, respectively. The blank experiment for methanol showed ~5% loss for evaporation, while for formaldehyde the loss was negligible. For the TiO_2 electrode, the COD removal efficiency quickly increased to 15% in the first half hour of illumination. For the next 4.5 h, the efficiency slowly increased up to 20%. In the case of the WO_3/TiO_2 electrode, the COD removal efficiency reached 17% in the first half hour and 35% after 5 h. The COD formaldehyde removal efficiency shows a more linear increment rate reaching 34% and 42% after 5 h for TiO_2 and WO_3/TiO_2 electrodes, respectively. The COD removal efficiency difference for formaldehyde is small enough that it can only be seen at long times, whereas the composite WO_3/TiO_2 shows a more significant enhancement at removal of methanol.

4. CONCLUSIONS

In this work, we demonstrated a practical synthetic approach to create tubular WO_3 nanostructures using TiO_2 nanotubes as a substrate. These materials were employed as photoanodes in a photoelectrochemical cell for the degradation of organic pollutants and the simultaneous generation of photocurrent for hydrogen production. We demonstrated that each process in the operation of the photoelectrochemical cell can be improved without jeopardizing the other processes, which resulted in an overall efficiency improvement. We showed that tubular WO_3/TiO_2 nanocomposites improved the solar spectrum absorption as well as the photodegradation and photocurrent efficiencies, as compared to TiO_2 and WO_3 alone. Diffuse reflectance spectra show an improvement in the visible absorption relative to bare TiO_2 nanotubes and in the UV absorption relative to bare WO_3 films. Comparing the absorption spectrum and IPCE plot, we can conclude that for all the wavelengths at which the composite electrodes absorb photons a photocurrent is generated. The results of this work suggest that the optimization of the nanostructure and composition of these composite materials improve the photogenerated carrier transport and the absorption pathways, resulting in higher IPCE efficiencies. In addition, the electrode/electrolyte interfacial transfer was improved by incorporating the fast and irreversible oxidation of organic pollutants, resulting in higher photocurrents that can be used to drive reduction reactions. These WO_3/TiO_2 nanostructured and related materials are promising candidates for practical photochemical reactors that drive simultaneous useful reactions, such as water reduction (H_2 production) and oxidation of pollutants.

■ ASSOCIATED CONTENT

Supporting Information

Representative EDS spectrum of WO_3/TiO_2 materials is shown in Figure S-1. A SEM image of WO_3 electrodeposited on Ti foil is shown in Figure S-2, and SEM images of the edge of WO_3/TiO_2 materials are shown in Figure S-3. This material is available free of charge via the Internet at http://pubs.acs.org.

■ AUTHOR INFORMATION

Corresponding Author

*E-mail: krreyes@sandia.gov.

Notes

The authors declare no competing financial interest.

■ ACKNOWLEDGMENTS

The authors thank Zachary D. Stephens for his technical work during the summer 2012, Dr. Vitalie Stavila for his valuable help in the XRD data collection, and Jeffery M. Chames for the SEM and EDS data collection. The authors also want to thank Brian Patterson, Paul Schrader, and Dr. John Goldsmith for their contribution in the instrumental setup for IPCE measurements. This work was funded by the Early Career Laboratory Directed Research and Development program at Sandia National Laboratories, a multi-program laboratory managed and operated by Sandia Corporation, a wholly owned subsidiary of Lockheed Martin Corporation, for the U.S. Department of Energy's National Nuclear Security Administration under contract DE-AC04-94AL85000.

■ REFERENCES

(1) Shankar, K.; Basham, J. I.; Allam, N. K.; Varghese, O. K.; Mor, G. K.; Feng, X. J.; Paulose, M.; Seabold, J. A.; Choi, K. S.; Grimes, C. A. *J. Phys. Chem. C* **2009**, *113*, 6327−6359.
(2) Ilieva, M.; Nakova, A.; Tsakova, V. *J. Appl. Electrochem.* **2012**, *42*, 121−129.
(3) Shankar, K.; Basham, J. I.; Allam, N. K.; Varghese, O. K.; Mor, G. K.; Feng, X.; Paulose, M.; Seabold, J. A.; Choi, K.-S.; Grimes, C. A. *J. Phys. Chem. C* **2009**, *113*, 6327−6359.
(4) Kamat, P. V. *J. Phys. Chem. C* **2007**, *111*, 2834−2860.
(5) Boettcher, S. W.; Spurgeon, J. M.; Putnam, M. C.; Warren, E. L.; Turner-Evans, D. B.; Kelzenberg, M. D.; Maiolo, J. R.; Atwater, H. A.; Lewis, N. S. *Science* **2010**, *327*, 185−187.
(6) Spurgeon, J. M.; Plass, K. E.; Kayes, B. M.; Brunschwig, B. S.; Atwater, H. A.; Lewis, N. S. *Appl. Phys. Lett.* **2008**, *93*, 032112.
(7) Kayes, B. M.; Spurgeon, J. M.; Sadler, T. C.; Lewis, N. S.; Atwater, H. A. *Proc. IEEE* **2006**, *1*, 221−224.
(8) Reyes-Gil, K. R.; Spurgeon, J. M.; Lewis, N. S. *Proc. SPIE* **2009**, *7408*, 740826.
(9) Mor, G. K.; Shankar, K.; Paulose, M.; Varghese, O. K.; Grimes, C. A. *Nano Lett.* **2006**, *6*, 215−218.
(10) Beranek, R.; Tsuchiya, H.; Sugishima, T.; Macak, J. M.; Taveira, L.; Fujimoto, S.; Kisch, H.; Schmuki, P. *Appl. Phys. Lett.* **2005**, *87*, 243114.
(11) Kongkanand, A.; Dominguez, R. M.; Kamat, P. V. *Nano Lett.* **2007**, *7*, 676.
(12) Reyes-Gil, K. R.; Wiggenhorn, C.; Brunschwig, B. S.; Lewis, N. S. *J. Phys. Chem. C* **2013**, *117*, 14947−14957.
(13) Benoit, A.; Paramasivam, I.; Nah, Y. C.; Roy, P.; Schmuki, P. *Electrochem. Commun.* **2009**, *11*, 728−732.
(14) Nah, Y.-C.; Ghicov, A.; Kim, D.; Berger, S.; Schmuki, P. *J. Am. Chem. Soc.* **2008**, *130*, 16154−16155.
(15) Nah, Y.-C.; Ghicov, A.; Kim, D.; Schmuki, P. *Electrochem. Commun.* **2008**, *10*, 1777−1780.
(16) Paulose, M.; Shankar, K.; Yoriya, S.; Prakasam, H. E.; Varghese, O. K.; Mor, G. K.; Latempa, T. J.; Fitzgerald, A.; Grimes, C. A. *J. Phys. Chem. B* **2006**, *110*, 16179−16184.
(17) Shankar, K.; Mor, G. K.; Prakasam, H. E.; Yoriya, S.; Paulose, M.; Varghese, O. K.; Grimes, C. A. *Nanotechnology* **2007**, *18*, 065707.
(18) Kaneko, M.; Ueno, H.; Ohnuki, K.; Horikawa, M.; Saito, R.; Nemoto, J. *Biosens. Bioelectron.* **2007**, *23*, 140−143.

(19) Chamousis, R. L.; Osterloh, F. E. *ChemSusChem.* **2012**, *5*, 1482−1487.
(20) Li, Y.; Lu, G.; Li, S. *Chemosphere* **2003**, *52*, 843−850.
(21) Roy, P.; Berger, S.; Schmuki, P. *Angew. Chem., Int. Ed.* **2011**, *50*, 2904−2939.
(22) Yang, M.; Shrestha, N. K.; Schmuki, P. *Electrochem. Commun.* **2009**, *11*, 1908−1911.
(23) Lai, C. W.; Sreekantan, S.; San, E. P. *J. Mater. Res.* **2012**, *27*, 1695−1704.
(24) Somasundaram, S.; Chenthamarakshan, C. R.; Tacconi, N. R. d.; Basit, N. A.; Rajeshwar, K. *Electrochem. Commun.* **2006**, *8*, 539−543.
(25) Pauporté, T. *J. Electrochem. Soc.* **2002**, *149*, C539−C545.
(26) Howard, C. J.; Luca, V.; Knight, K. S. *J. Phys.: Condens. Matter* **2002**, *14*, 377−388.
(27) Xin, G.; Guo, W.; Ma, T. *Appl. Surf. Sci.* **2009**, *256*, 165−169.
(28) Hong, S. J.; Jun, H.; Lee, J. S. *Scr. Mater.* **2010**, *63*, 757−760.
(29) Bamwenda, G. R.; Arakawa, H. *Appl. Catal. A* **2001**, *210*, 181−191.
(30) Yang, B.; Barnes, P. R. F.; Zhang, Y.; Luca, V. *Catal. Lett.* **2007**, *118*, 280−284.
(31) Georgieva, J.; Armyanov, S.; Valova, E.; Poulios, I.; Sotiropoulos, S. *Electrochem. Commun.* **2007**, *9*, 365−370.
(32) Yang, B.; Zhang, Y.; Drabarek, E.; Barnes, P. R. F.; Luca, V. *Chem. Mater.* **2007**, *19*, 5664−5672.
(33) Ostachaviciute, S.; Baltrusaitis, J.; Valatka, E. *J. Appl. Electrochem.* **2010**, *40*, 1337−1347.
(34) Habazaki, H.; Hayashi, Y.; Konno, H. *Electrochim. Acta* **2002**, *47*, 4181−4188.
(35) Santato, C.; Odziemkowski, M.; Ulmann, M.; Augustynski, J. *J. Am. Chem. Soc.* **2001**, *123*, 10639−10649.
(36) Wahl, A.; Augustynski, J. *J. Phys. Chem. B* **1998**, *102*, 7820−7828.